# **OPEN ACCESS**



# Bulk Properties of Pickup Ions Derived from the Ulysses Solar Wind Ion Composition Spectrometer Data

William P. Smith<sup>1</sup>, Kyle Renfroe<sup>2</sup>, Nikolai V. Pogorelov<sup>1,2</sup>, Ming Zhang<sup>3</sup>, Michael Gedalin<sup>4</sup>, and Tae K. Kim<sup>1</sup> Center for Space Plasma and Aeronomic Research, The University of Alabama in Huntsville, Huntsville, AL 35805, USA; np0002@uah.edu

Department of Space Science, The University of Alabama in Huntsville, Huntsville, AL 35805, USA

Department of Physics and Astronomy, Florida Institute of Technology, Melbourne, FL, USA

Ben-Gurion University of the Negev, Beer Sheva, Israel

Received 2022 March 29; revised 2022 May 23; accepted 2022 May 25; published 2022 July 8

#### Abstract

Nonthermal, pickup ions (PUIs) represent an energetic component of the solar wind (SW). While a number of theoretical models have been proposed to describe the PUI flow, of major importance are in situ measurements providing us with the vital source of model validation. The Solar Wind Ion Composition Spectrometer (SWICS) instrument on board the Ulysses spacecraft was specifically designed for this purpose. Zhang et al. proposed a new, accurate method for the derivation of ion velocity distribution function in the SW frame on the basis of count rates collected by SWICS. We calculate the moments of these distribution functions for protons (H<sup>+</sup>) and He<sup>+</sup> ions along the Ulysses trajectory for a period of 2 months including the Halloween 2003 solar storm. This gives us the time distributions of PUI density and temperature. We compare these with the results obtained earlier for the same interval of time, in which the ion spectra are converted to the SW frame using the narrow-beam approximation. Substantial differences are identified, which are of importance for the interpretation of PUI distributions in the 3D, time-dependent heliosphere. We also choose one of the shocks crossed by Ulysses during this time interval and analyze the distribution functions and PUI bulk properties in front of and behind it. The results are compared with the test-particle calculations and diffusive shock acceleration theory.

Unified Astronomy Thesaurus concepts: Solar wind (1534); Pickup ions (1239)

#### 1. Introduction

The interaction between the solar wind (SW) and the local interstellar medium (LISM) is an important process that forms a tangential discontinuity (the heliopause (HP)) between the two plasma flows. From the viewpoint of ideal MHD, the HP is not penetrable for both SW and LISM plasma. Since the SW becomes superfast magnetosonic already at distances of about 10–15  $R_{\odot}$ , the heliospheric termination shock (TS) is ultimately formed where SW plasma is decelerated to subfast magnetosonic velocities due to the HP presence. Voyager 1 and 2 (V 1 and V 2) crossed the TS at 94 and 84 au, respectively. The region between the TS and HP is called the inner heliosheath (IHS). The SW-LISM interaction is greatly affected by charge exchange between the SW ions and interstellar neutral atoms. This is because the LISM ionization ratio is about 30%. LISM neutral atoms, especially H and He, can propagate deep into the heliosphere (Wallis 1971, 1975). Charge exchange between SW ions and interstellar H atoms creates secondary neutral atoms, which propagate outwards and can even penetrate into the LISM (Gruntman 1982). In addition, strongly nonthermal, pickup ions (PUIs) are created in the heliosphere (Möbius et al. 1985; Gloeckler et al. 2009). As the distribution function of PUIs evolves, waves/turbulence is generated, which heats up the thermal SW ions, which is clearly seen in V 1 and V 2 observations (Richardson et al. 2008) and related numerical modeling (e.g., Gedalin et al. 2021, and references therein). For this reason, the expansion of the thermal SW protons is not adiabatic and their temperature starts to increase at heliocentric

Original content from this work may be used under the terms of the Creative Commons Attribution 4.0 licence. Any further distribution of this work must maintain attribution to the author(s) and the title of the work, journal citation and DOI.

distances exceeding ~15 au (Richardson & Smith 2003). As the spacecraft move farther from the Sun in the direction of the TS, the contribution of PUIs to the total pressure (the sum of the thermal and magnetic pressures) becomes dominant (Burlaga et al. 1994; Richardson et al. 1995; Zank 1999; Zank et al. 2014).

Numerical models to account for the presence of PUIs require observational validation. Although the effect of PUIs on the SW flow is especially strong in the outer heliosphere (OH, the SW region where the PUI pressure is dominant over the thermal plasma pressure), PUIs are detected at 1 au by the Advanced Composition Explorer (Möbius et al. 2015) and, at different radial distances (1.35–5.4 au) and heliolatitudes (up to  $\sim 80^{\circ}$ ), by Ulysses (von Steiger et al. 2001; Bzowski et al. 2008). New Horizons (NH) is now at  $\sim \!\!50$  au from the Sun with the information on PUIs provided by two different instruments (McComas et al. 2017; Kollmann et al. 2019), although no magnetic field measurements are available.

Ulysses data obtained with the Solar Wind Ion Composition Spectrometer (SWICS) remain an invaluable source of information about PUIs properties, as well as other quantities describing the SW plasma flow. The interplanetary magnetic field is measured by the Ulysses magnetometer (MAG). SWICS measurements have been of profound importance for our understanding of the properties and energy distribution of SW ions in the energy range between 0.65 and 60 keV per unit charge (Gloeckler 1990, 1996).

Interpretation of SWICS measurements is a challenging task because the measurements of particle distributions strongly depend on the angle between the SW flow direction and the instrument field of view. This is not surprising, since the ion velocity distribution function (VDF) is anisotropic in the spacecraft frame, which is especially prominent for relatively

low-energy ions, such as the thermal SW ions and PUIs. Ulysses measurements make it possible to derive the ion distributions integrated over the instrument field of view averaged over the full spin. These integrated distributions cannot be directly used for deriving the ion VDFs and the bulk properties of SW ions. Zhang et al. (2019) proposed a new approach to recover the ion VDF in the SW frame. This approach offers an improvement upon the standard narrowbeam approximation (von Steiger et al. 2000).

The essence of the narrow-beam approximation is the following. If one assumes that the SW can be represented as a delta-function of angle spread, or by a 1D velocity distribution along the Sun-spacecraft line, it is possible to derive the distribution function with respect to the SW velocity direction in the spacecraft frame from measurements of particle count rates in all energy channels. Distribution functions being invariant with respect to the Galilean transformations, Gloeckler et al. (1995) obtained them in the SW frame by shifting velocity by the bulk SW speed,  $V_{\rm SW}$ . The narrow-beam approximation is reasonable for the thermal SW core because SW thermal speed is much smaller than the bulk velocity. However, it is not appropriate for PUIs, whose distribution functions have a much broader spread in the velocity space. The Ulysses SWICS instrument has a wide field of view, and the spacecraft is spinning at  $\sim$ 12 rpm, which is much faster than the time needed to accumulate enough counts for PUI VDF measurements. SWICS can see particles coming from a wide range of angular directions in each measurement readout. In the spacecraft frame, the ion flux is up to a few orders of magnitude higher in the sunward direction than in the antisunward direction, which makes it difficult to reliably convert the raw count rate measurements into the distribution functions. In contrast, Zhang et al. (2019) assumed that the particle distribution function is nearly isotropic in the SW frame inside the instrument field of view. This made it possible to derive more reliable VDFs, especially for PUIs. It is expected that the bulk properties of the SW plasma and PUIs, obtained using the newly calculated VDFs, will also be determined with higher accuracy.

In this paper, we build on the results of Zhang et al. (2019) to derive the bulk properties of PUIs. This is done by calculating the moments of the distribution functions for protons (H+) and He+ ions along the Ulysses trajectory each 6 hr consecutively over the period of 2 months (Day of the year (DOY) 290–350, 2003) including the Halloween 2003 solar storm. Our results are compared with the previous analysis by Intriligator et al. (2012), where the particle spectra are converted to the SW frame using the narrow-beam approximation, and a noticeable difference is observed.

In addition, we identify a clear fast-mode MHD shock that occurred during the considered solar event period and analyze the change in the H<sup>+</sup> and He<sup>+</sup> distribution functions, and the corresponding bulk PUI properties, across it. We determine the bulk properties of the thermal SW from the Ulysses Solar Wind Observations Over the Poles of the Sun (SWOOPS) instrument. Our results are of importance for the clear identification of processes occurring in the quiet SW and near shocks propagating through it. Integrating the particle spectra of ions in the SW allows for the determination of the bulk plasma properties, such as the PUI density and temperature. These results are important for the validation of simulations of the SW-LISM interaction, as including the effects of interstellar

PUIs in these simulations can significantly modify the energy balance in the OH.

The paper is structured as follows. In Section 2 we briefly describe the data obtained from the SWOOPS and SWICS instruments on board Ulysses. Section 3 gives an overview of the methods we used to perform the data analysis. The results of our calculation of the PUI bulk properties are analyzed in Section 4. We compare the results based on the VDFs obtained with the methodology of Zhang et al. (2019) and those based on the narrow beam. In conclusions, we discuss the applicability of our method and challenges with the derivation of SW bulk properties in the time intervals of rapid SW velocity changes due to coronal mass ejections (CMEs), corotating interaction regions, shock vicinity, etc.

# 2. Data from the Ulysses SWICS and SWOOPS

The data used in this project were measured by the SWICS, SWOOPS, and MAG instruments on board the Ulysses spacecraft during October and November of 2003, when Ulysses was at heliospheric distance of about 5 au. The SWICS instrument measures the elemental and ionic-charge composition, temperature, and mean speeds of SW ions. SWICS covers the interval of speeds from 175 to 1280 km s<sup>-1</sup> and energy per charge from 0.16 to  $59.6 \,\mathrm{keV}$   $\mathrm{e}^{-1}$ . The time cadence is approximately 13 minutes. The SWOOPS instrument is used to derive the velocity, density, and temperature of the thermal SW plasma. Particle data from SWICS can be used to construct the VDFs, whereas the SW velocity data from SWOOPS are necessary to convert the VDFs to the SW frame, as shown in Zhang et al. (2019). Any transformation of VDFs from the spacecraft frame to the SW frame is reliable only when the SW speed is not changing rapidly within a time interval chosen to accumulate those VDFs. In this paper, the accumulation time is 6 hr. If this condition is not satisfied, the velocities obtained can be considered as average velocities, which may affect the resulting bulk temperatures (von Steiger et al. 2000).

Figure 1 shows three different populations of protons in the plasma (SW-)frame VDF obtained for DOY 290, 2003. All further VDFs are also shown in the SW frame. The thermal SW core appears in the VDF as a near-Maxwellian distribution, which contains the vast majority of ions. It is followed by a relatively flat region containing interstellar PUIs generated mostly by charge exchange and photoionization at the heliospheric distances we consider. When an interstellar neutral atom enters the heliosphere, it can experience resonant charge exchange with a same-nucleus SW ion. As a result, a new ion is created with the properties of the parent interstellar atom. This newly created ion (a PUI), being inserted into the SW flow, immediately experiences motional electric field  $E = -v_{\rm rel} \times B$ , where  $v_{\rm rel}$  and  $\boldsymbol{\mathit{B}}$  are the relative velocity and magnetic field vector, respectively. The electric force acts as long as the relative bulk velocity vanishes. PUIs are quickly scattered onto a spherical shell distribution centered at the SW velocity, with the radius of the shell also equal to  $V_{SW}$ . As PUIs propagate further downstream the distribution function acquires a filledshell distribution described by Vasyliunas & Siscoe (1976). The full distribution function also involves the thermal, core SW ions and energetic tales corresponding to PUIs accelerated at interplanetary shocks. The PUI "plateau" begins at the edge of the near-Maxwellian curve of the thermal SW core, which covers up any PUIs at lower energies. The furthest extent of the PUI plateau occurs at approximately twice the SW speed in the

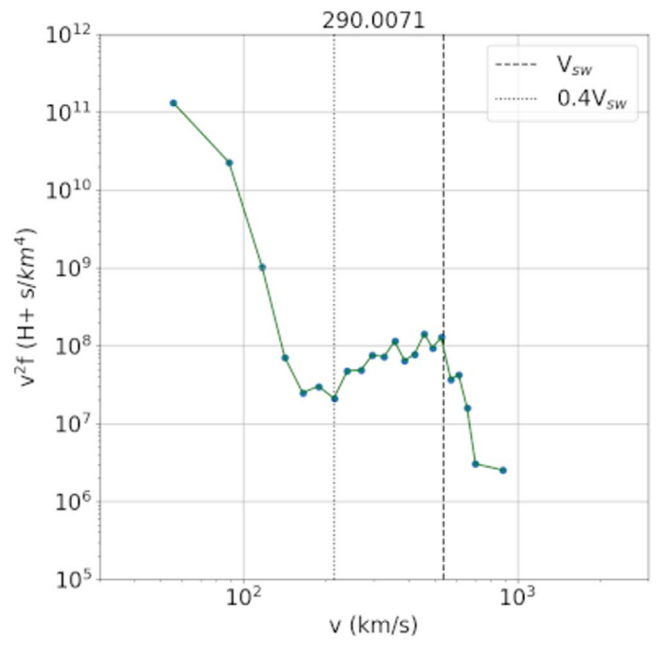


**Figure 1.** The SW velocity distribution function in the SW frame on DOY 290, 2003 shows different proton populations: the thermal core, PUIs, and high-energy power-law tail. This function corresponds to a very slow SW speed variation, making PUIs easily identifiable. The vertical lines are drawn for  $v = 0.4~V_{\rm SW}$  and  $v = V_{\rm SW} = 537.7~{\rm km~s}^{-1}$ .

spacecraft frame, or at the SW speed in the plasma frame. The number of particles contained in the PUI velocity range is much lower than that in the thermal SW core, but much higher than the number of particles contained in the superthermal tail, which follows the PUI range. The superthermal tail contains a small number of very high-energy particles, but it is not subject of this study.

Rapid changes associated, e.g., with CMEs can cause difficulties in the interpretation of VDFs. An example of such a function calculated on DOY 319 in the vicinity of a shock at the leading edge of a CME is shown in Figure 2. As a consequence, the integration of VDFs taken from within CMEs must be treated slightly differently than for those outside them (see Section 3). In particular, the near-Maxwellian curve of the thermal SW core expands to higher velocities. so that the PUI plateau becomes indistinguishable. The integration limits for such cases are hard to determine accurately due to the uncertain boundaries of the PUI plateau. However, there still exist approaches that allow us to identify PUIs. They are discussed Sections 3.2 and 3.3.

It is important to mention that the 6 hr averaged VDFs produce inaccuracies when the SW velocity is changing very rapidly, such as when a shock front passes over the spacecraft. This is due to the fact that the construction of VDFs and the method of converting them to the SW frame both assume that the SW speed is constant, on average, during the collection period for each individual distribution function. However, this only occurs for a small fraction of the distribution functions, even during the active Sun intervals. As a CME passage can last 1–2 days, we have four to eight 6 hr distribution functions inside them.

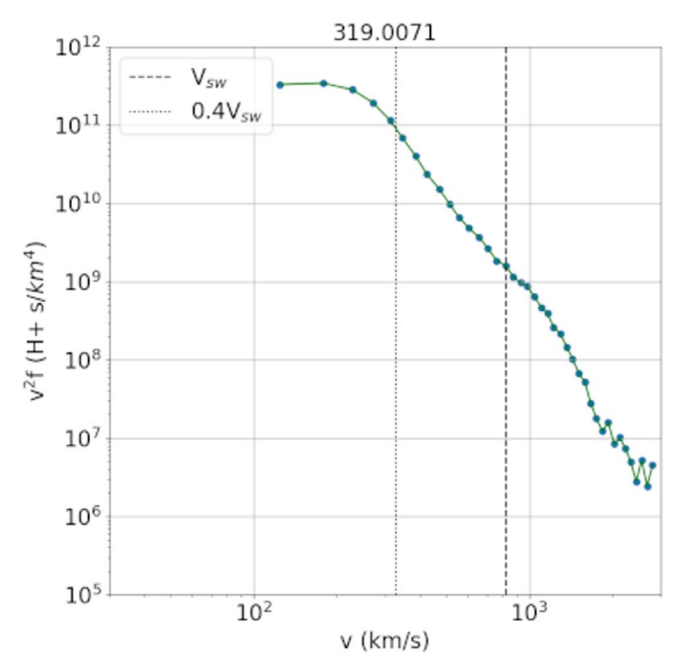


**Figure 2.** The DOY 319.0 distribution function in the SW frame with indistinguishable PUI plateau caused by a rapid variation of the SW velocity due to the shock propagation. The vertical lines are drawn for  $v = 0.4 V_{\rm SW}$  and  $v = V_{\rm SW} = 820.7 ~\rm km ~s^{-1}$ .

# 3. Integration of the Distribution Functions

### 3.1. Standard Cases

The bulk properties of PUIs can be calculated by taking moments of the ion VDFs. In this way, we can determine the ion density, temperature, pressure, etc. Since the VDFs we use are isotropic and given in the SW frame, we have the following formulae for the number density:

$$n = \int_{-\infty}^{\infty} \int_{-\infty}^{\infty} \int_{-\infty}^{\infty} f(\sqrt{v_x^2 + v_y^2 + v_z^2}) dv_x dv_y dv_z$$
  
=  $\int_{0}^{\pi} dv_\theta \int_{0}^{2\pi} dv_\phi \int_{0}^{\infty} v_R^2 f(v_R) dv_R = 4\pi \int_{0}^{\infty} v^2 f(v) dv,$  (1)

where f(v) is an isotropic VDF in the spherical coordinate system and integration is performed over spherical coordinates in the velocity space.

The thermodynamic temperature is therefore

$$T = \frac{4\pi m}{3kn} \int_0^\infty v^4 f(v) dv, \tag{2}$$

where m and k are the ion mass and the Boltzmann constant, respectively.

To achieve our goal of finding  $n_{\rm PUI}$  and  $T_{\rm PUI}$ , we need to identify the velocity interval of PUIs in each measured VDF. According to Vasyliunas & Siscoe (1976), PUIs should be distinguishable from the Maxwellian or, possibly, Lorentzian core ions as a plateau-like region with the slope considerably smaller than that of the adjacent (in the velocity space) thermal ions (see, e.g., Figure 1). Thus, the integration limits can be found by determining the extent of such PUI plateau. It should be noticed that the velocity interval belonging to PUIs is necessarily contaminated by the presence of thermal ions in the same range (compare this with Figure 1). As mentioned in the previous section (see Figure 2) this contamination is sometimes

rather severe. The lower integration limit should be chosen especially carefully, as picking a limit that is too small will include part of the thermal SW core ions, the VDF of which is rapidly growing as v decreases. This typically results in a substantial overestimation of PUI density. In Intriligator et al. (2012), the integration limits are rigidly set at 0.4  $V_{\rm SW}$  and  $V_{\rm SW}$ (1.4  $V_{SW}$  and 2  $V_{SW}$  in the spacecraft frame) for the entire time interval of data analysis. Of course, the SW speed is different for each 6 hr period and is taken from the SWOOPS data. The integration limits chosen like that are shown in Figure 1 and 2. The upper limit of integration corresponds to the theoretical value based on the assumption that the initial PUI VDF is a spherical shell with radius  $V_{SW}$ , i.e., possible velocities are in the range between 0 and  $V_{SW}$ . Of course, the core SW dominates at small velocities, which requires the lower cutoff for PUIs be a fraction of  $V_{SW}$ .

The inspection of the measured VDFs shows that the factor of 0.4 is not optimal even in the cases when a plateau is clearly identifiable. For this reason, we manually analyzed each VDF to set appropriate cutoff values. This is especially important because the cutoff limits (in terms of  $V_{\rm SW}$ ) are different for the quiet SW and in the presence of CMEs. This approach to the determination of the integration limits is obligatory during solar active periods when the overall distribution functions can change significantly, such as those measured during the 2 month period involving five CMEs, which we are analyzing in this paper. Of course, the manual analysis is excessively time consuming to be used for longer intervals of time. We plan to automate this process in the future and apply it for the whole Ulysses mission lifetime.

# 3.2. Subtracting VDFs of the Core Ions

In the situations when a VDF does not exhibit a clearly distinguishable PUI plateau, like, e.g., in Figure 2, additional measures should be undertaken to process the measured distribution function. The reason of such behavior is the presence of low- and high-speed streams following each other and the possibility of ion acceleration by shocks crossing the spacecraft trajectory. As a result, the lower cutoff boundary can be hard to identify. Here we follow the approach proposed by Zhang et al. (2019). Since the core SW ions are assumed to be accelerated, we can approximate their VDF with a Lorentzian (kappa) distribution function:

$$f(v) = g \left[ 1 + \left( \frac{v^2}{\kappa w^2} \right) \right]^{-\kappa - 1},\tag{3}$$

where w is the thermal velocity describing the width of the core SW distribution and  $\kappa$  is adjusted to fit each VDF. As  $\kappa \to \infty$ , the distribution of the thermal ions approaches the Maxwellian distribution.

Thus, in the cases where the PUI plateau is either indistinguishable or unclear, we fit a number of points belonging in a particular VDF to the thermal SW ions by a kappa distribution function (3) multiplied by  $v^2$ . The values of w,  $\kappa$ , and the proportionality constant, g, were the three parameters we varied in our fitting procedure. The details are shown in Figure 3 and later in Figure 7 (*right panel*), the latter corresponding to DOY 333.51. Since the points with lower velocities are less accurate, the choice of the leftmost point for fitting plays a minor role. As a change in the VDF slope is seen even in such complicated cases, the rightmost fitting point was

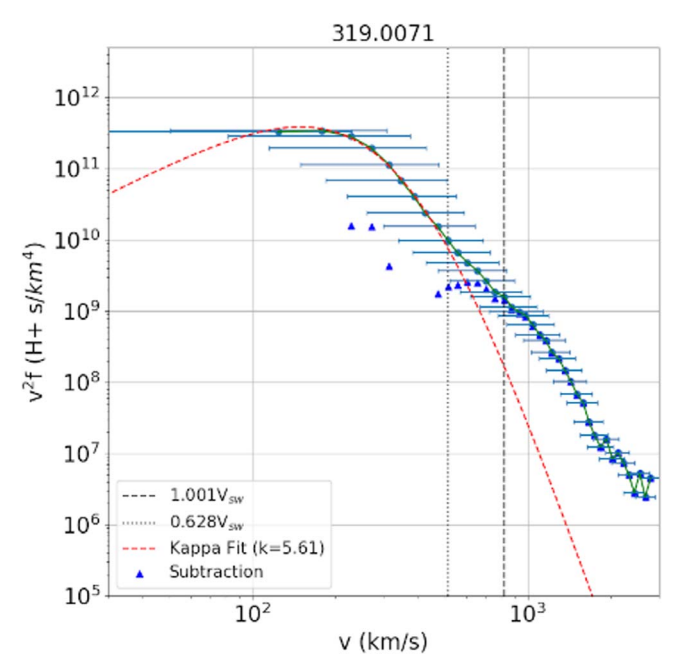


**Figure 3.** DOY 319 where thermal SW ions are fit to a kappa distribution function and subtracted from the original distribution function. The rectangles indicate the full distribution. The kappa distribution function is shown with the red dashed line. The triangles are obtained by subtraction of the kappa distribution from the full distribution function. Here  $V_{\rm SW}=820.7~{\rm km~s}^{-1}$ .

selected to lie a few points to the left of the slope change point. This is done to eliminate the uncertainty in the identification of points belonging to the core SW. In a few cases when no noticeable change of slope was observed, the rightmost point was chosen so that the integration of the kappa distribution agreed with the total proton density measured by SWOOPS. Afterwards, the kappa distribution was fitted to the points bounded by this range. By subtracting the distribution of thermal SW ion from the full VDF, we were able to reveal a PUI plateau. In Figure 3, which corresponds to DOY 319, the input distribution function is shown with rectangles, each accompanied with the corresponding horizontal error bars, connected by the green line. The width of these error bar indicates the velocity range where the response function value in each channel is above 10% of the peak value in it. The width is higher at lower velocities because the thermal spread becomes more pronounced. The red dashed line represents a fit with the kappa function, and the triangles show the difference between them. The resulting VDF demonstrates a clear plateau with left and right cutoff velocities easily identifiable. We are not worried by the presence of outliers at smaller velocities. They are due to the differences between two very large numbers and are consistent with the uncertainty of measurements. In addition, they do not belong to the PUI velocity range. Our approach is especially effective during 6 hr intervals behind transient shocks.

# 3.3. Moments of the He<sup>+</sup> Distribution Functions

The integration of the He<sup>+</sup> VDFs is easier because the overwhelming majority of He<sup>+</sup> ions in the SW are PUIs born mostly due to the ionization of He atoms arriving into the inner heliosphere from the LISM. For this reason, we simply integrate the He<sup>+</sup> VDFs obtained following Zhang et al. (2019) over the entire velocity range.

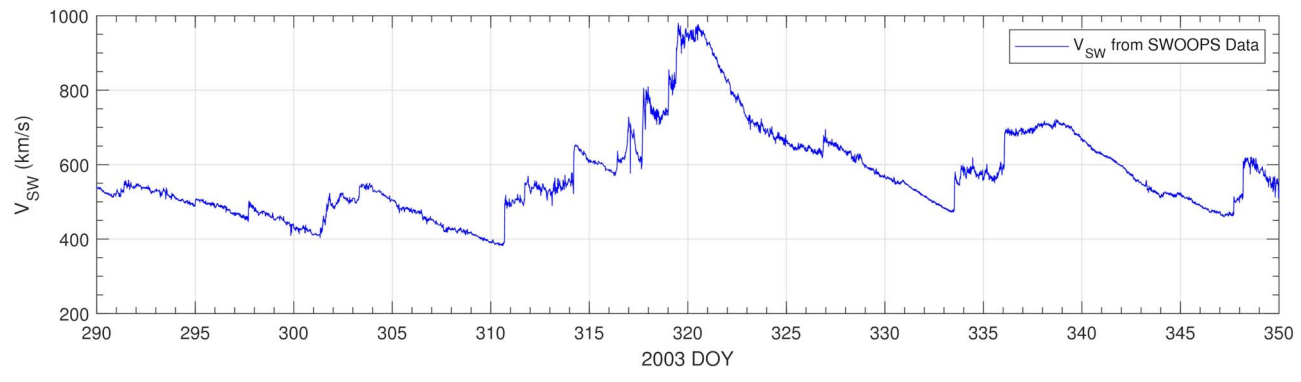


Figure 4. Solar wind speed from the Ulysses SWOOPS data.

## 4. The Results and Their Discussion

# 4.1. Comparison of PUI Bulk Properties with Those Obtained Using the Narrow-beam Approximation

We integrate the VDFs to determine the PUI density and temperature over a 2 month time period of October to November 2003, which encompasses the so-called Halloween 2003 solar events. The distribution of the SW speed for this interval of time is taken from SWOOPS data (Figure 4). We chose this time period to test the effectiveness of our PUI identification methods during a solar active period when multiple CMEs pass over the spacecraft and strongly affect the SW plasma properties. Our results are shown in Figure 5 both for H<sup>+</sup> and He<sup>+</sup> PUIs. Note the five CMEs, which can be seen as sharp increases in the PUI density in the top panel of Figure 5. Five regions of enhanced SW plasma density are also seen in the SWOOPS data. They account for approximately 30% of the time period. However, rapid changes in velocity associated with shocks visible in Figure 4, are far less frequent. This makes most of the VDFs sufficiently accurate to derive the bulk properties of PUIs.

The choice of time interval allows us to compare our results for the pickup proton density and temperature with those presented earlier (Intriligator et al. 2012), where the narrow-beam approximation was used for converting the VDFs to the SW frame. In contrast, the approach of Zhang et al. (2019) involves deconvolutions of the instrument response function from the measurements and applies pseudomatrix inversions to derive the particle spectrum in the SW frame. The knowledge of the bulk PUI properties obtained from Ulysses data is important for understanding the PUI behavior in the time-dependent SW and can be used for validation of numerical simulations, which are now becoming abundant in the anticipation of the *IMAP* mission (McComas et al. 2018).

Figure 5 shows the results of such comparison. The density and temperature distributions for pickup protons (blue lines for our new analysis and red lines for the narrow-beam approximation) and pickup He<sup>+</sup> (green lines) are shown at the top and bottom panels, respectively. SWOOPS data for proton density are shown with the black line at the top panel. Our results for the PUI density and temperature are generally higher than those calculated using the narrow-beam approximation, especially during calmer periods. Notice also that the bulk properties of PUIs obtained with the narrow-beam approximation are much smoother. The differences between two different sets of distributions are almost entirely due to the differences in the input VDFs. It is of interest that the new derivation give rather consistent agreement with Intriligator et al. (2012) for the PUI

density, but not for their temperature, in the vicinity of CMEs. However, disagreement away from CMEs is universally substantial. The new, more precise approach to transforming the ion VDFs from the spacecraft to SW frame should be applied to the whole lifetime of the Ulysses mission.

### 4.2. PUI Behavior across a Collisionless Shock

The SW plasma is collisionless. The problem of shock crossing by PUIs in such an environment is one of the central problems of space physics. Observational data, such as those from Ulysses, provide us with important information on this subject. Although NH measurements (McComas et al. 2021), because they are performed in the region of much higher PUI density, are especially useful to study these phenomena, they are lacking magnetic fields, which makes the identification of shock properties difficult, if at all possible. Ulysses SWICS data, combined with the SWOOPS and MAG measurements, allow us to identify shocks and derive the PUI density and temperature behind them. It should be understood, however, that we can use only 6 days averaged VDFs. For this reason, the microscale, kinetic properties of shock crossings may be missed. Measurements already account for the ion acceleration and isotropization of their distributions behind shocks. Moreover, PUIs in front of the shock also arrive accelerated and partially isotropized. In this section we present a shock analysis based on the Ulysses data and compare it with the local, 1D test-particle (Gedalin et al. 2020) simulations in a small computational box, typically of 20 ion gyroradii, and the results of the diffusive acceleration theory (Drury 1983).

We chose a well-defined shock that crossed the Ulysses trajectory at DOY 333.5183 for our analysis. It is well seen in the Ulysses SWOOPS (Figure 4) and magnetometer data (Figure 6). The choice of this shock is also stipulated by the availability of VDFs on both sides of a shock avoiding the situation where such a shock is deeply inside the corresponding 6 hr interval. Since the SW properties in front of and behind the shock are known from the SWOOPS and MAG measurements, the MHD shock relations allowed us to calculate the shock normal n = (0.9150, 0.2659, 0.3036) and speed  $v_s = 574$  km s<sup>-1</sup>. The summary is presented in Table 1. This is a solid fastmode MHD shock with the fast magnetosonic Mach numbers,  $M_{\rm fn} = v_n/a_{\rm fn}$ , equal to 3.99 and 0.95 upstream and downstream, respectively. Here  $a_{fn}$  is the fast magnetosonic velocity in the direction normal to the shock. As required for fast-mode shocks, it is super-Alfvénic ( $M_{An} = v_n/a_{An} > 1$ ) on both sides of the shock. The compression ratio is 2.6. The shock moves faster than the SW in front of it, so the dominant (radial)

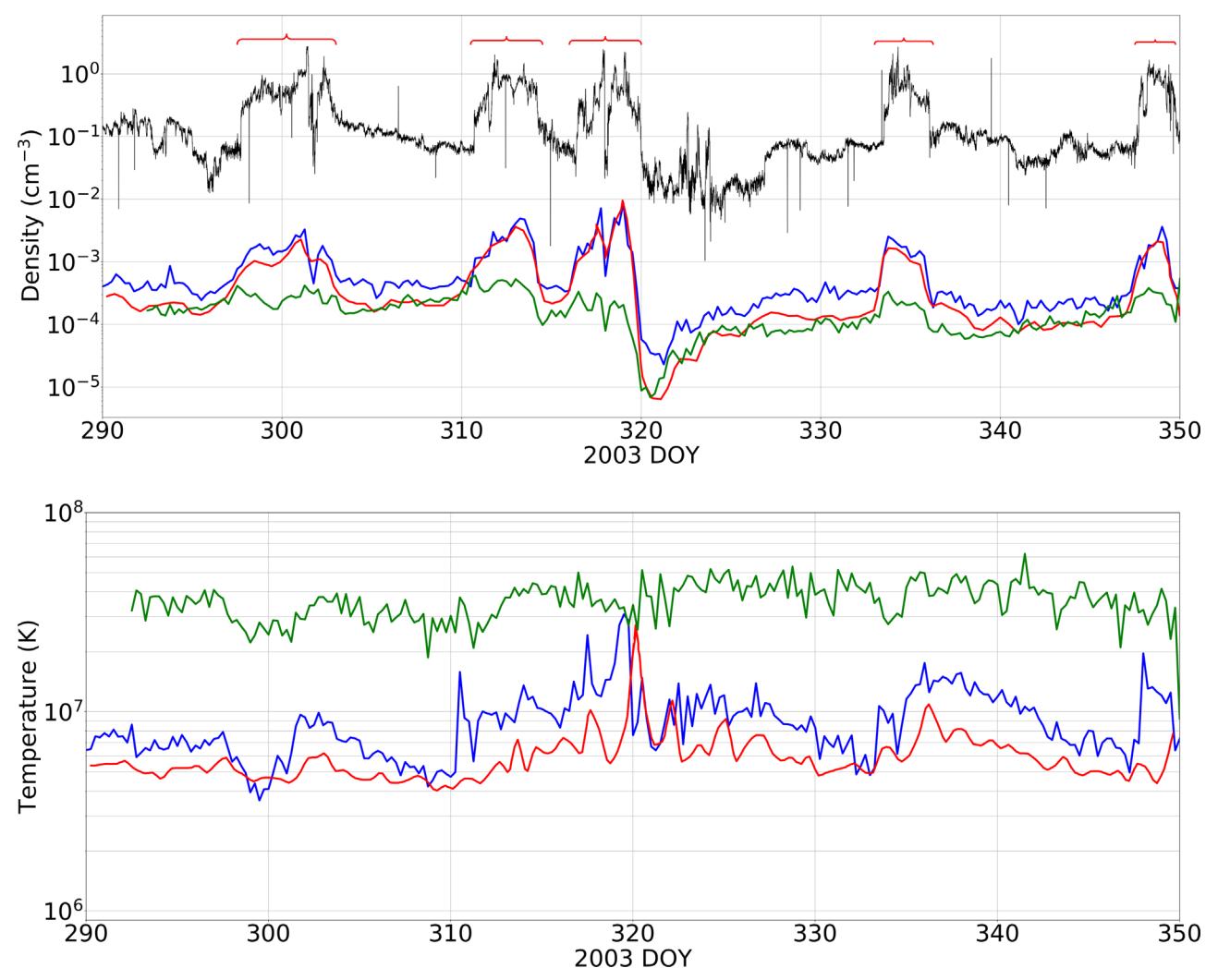


**Figure 5.** Comparison of the distributions of PUI density and temperature along the Ulysses trajectory obtained in this work (blue and green lines are used for for pickup protons and pickup He<sup>+</sup>, respectively) and those from the narrow-beam approximation for pickup protons (Intriligator et al. 2012; red lines). The proton density distribution from SWOOPS data is shown with black line. The red braces at the top panel show the stream interaction regions associated with CMEs.

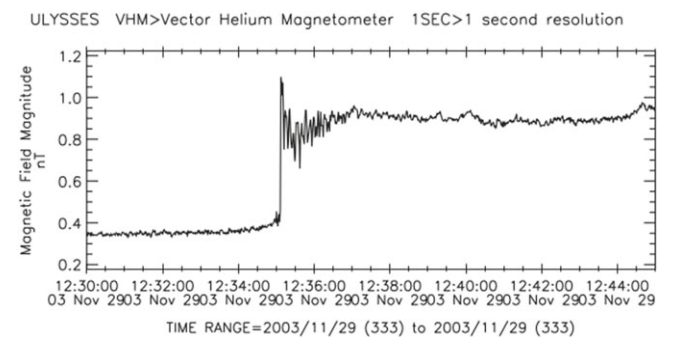


**Figure 6.** Magnetic field distribution in the vicinity of the chosen shock. Ulysses MAG data provided by CDAWeb at https://cdaweb.gsfc.nasa.gov.

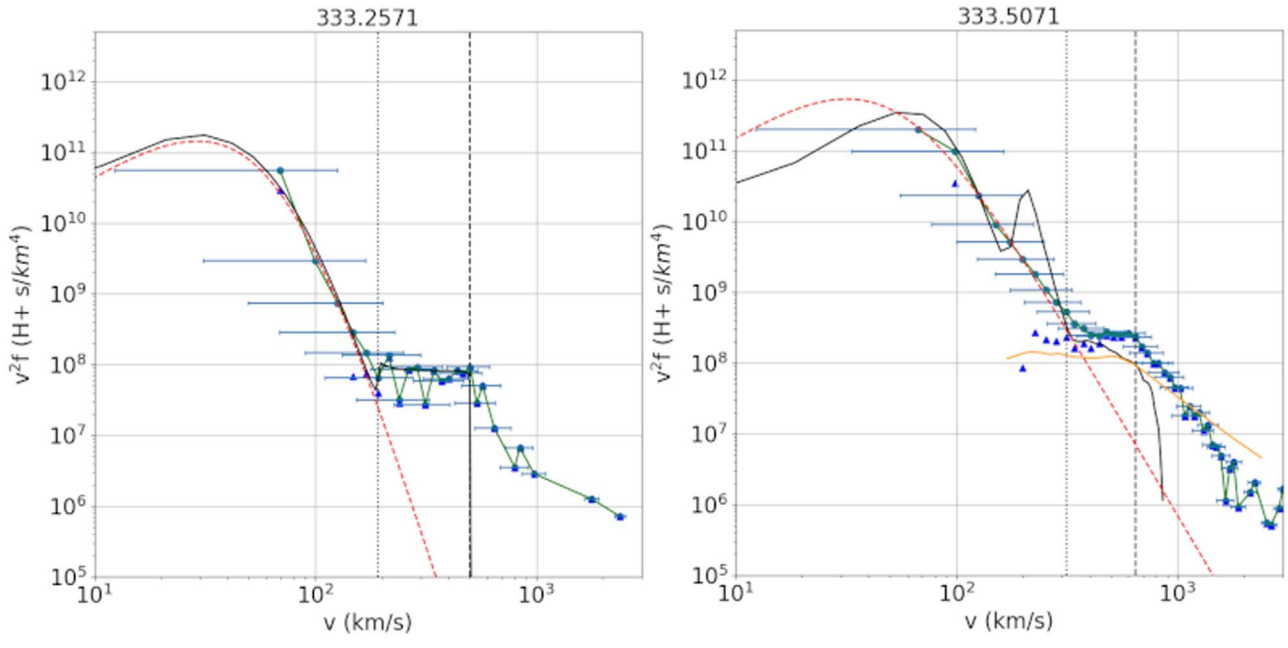
velocity component in the fixed frame increases across it. The normal velocity  $v_n$  with respect to the shock changes from 129.38 to 49.7 km s<sup>-1</sup>. Note that the shock normal, conventionally, is chosen to be directed from the lower density side of the shock to its higher density side. The velocity components in the table are provided in the spacecraft (RTN) frame. The *RTN* coordinate system is a local Cartesian system with the *R* axis along the Sun-spacecraft direction, the *T* axis is

 Table 1

 Properties of the Shock Occurring at DOY 333.5

Shock Properties	Upstream	Downstream
$(v_R, v_T, v_N) (\text{km s}^{-1})$	(483.80, 7.37, 0.90)	(558.77, 23.40, 23.37)
$(B_R, B_T, B_N)$ (nT)	(-0.029, 0.317, 0.127)	(-0.251, 0.743, 0.424)
$n  (\text{cm}^{-3})$	0.0932	0.2427
$n (\mathrm{H^+ PUI}) (\mathrm{cm^{-3}})$	$2.85 \times 10^{-4}$	$2.38 \times 10^{-3}$
$n (\mathrm{He^+ PUI}) (\mathrm{cm^{-3}})$	$1.3 \times 10^{-4}$	$2.84 \times 10^{-4}$
$T (H^+ PUI) (K)$	$5.2 \times 10^{6}$	$1.0 \times 10^{7}$
T (He <sup>+</sup> PUI) (K)	$3.5 \times 10^{7}$	$3.7 \times 10^{7}$
$p \text{ (pdyn cm}^{-2}\text{)}$	0.446	2.856
$\theta_{Bn}$	73.64 <sup>{</sup> °}	83.79 <sup>{</sup> °}
$v_{\rm A}~({\rm km~s^{-1}})$	24.46	39.48
$v_{An} (\text{km s}^{-1})$	6.89	4.27
$v_{\rm fn}~({\rm km~s}^{-1})$	32.45	52.19
$v_n  (\mathrm{km \ s}^{-1})$	129.37	49.70
$B_t$ (nT)	0.329	0.887
$M_{ m A}$	5.29	1.26
$M_{\mathrm{A}n}$	18.77	11.64
$M_{\mathrm{f}n}$	3.99	0.95

n = (0.9150, 0.2659, 0.3036) $v_s = 574 \text{ km s}^{-1}$ 



**Figure 7.** Proton spectra ahead (the left panel) and behind the shock (the right panel) that crossed the Ulysses trajectory on DOY 333.5. The distribution functions are shown with green lines and blue circles. The dashed red lines are used to fit the observational data in the thermal range with kappa distributions. The blue triangles show the difference between the input distribution function and the thermal ion distribution. The black line on the right panel shows the ion distribution obtained with the test-particle simulation. The smaller extremum in this distribution corresponds to reflected PUIs. The orange line shows the VDF based on the diffusive shock acceleration theory.

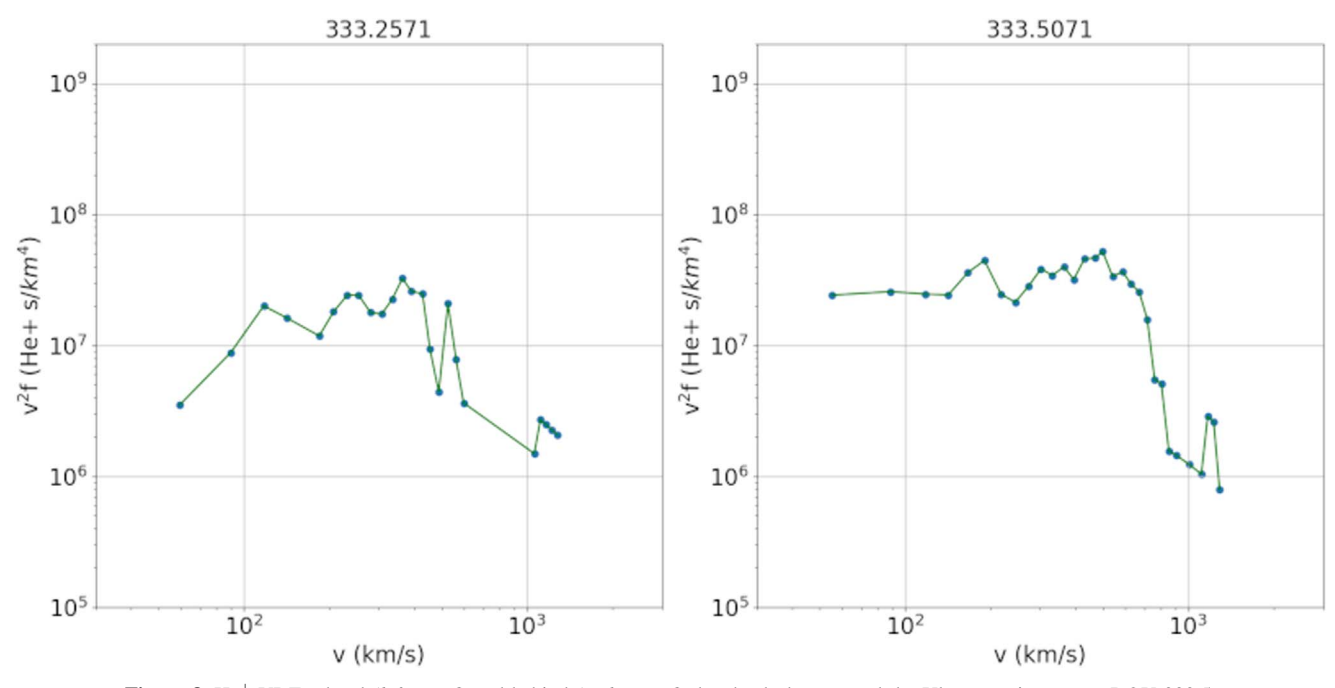


Figure 8. He<sup>+</sup> VDFs ahead (left panel) and behind (right panel) the shock that crossed the Ulysses trajectory on DOY 333.5.

in the direction of the Sun's rotation, and the N axis completes the right coordinate system.

To derive the density and temperature of pickup protons and He<sup>+</sup> ions we identified two 6 hr intervals predominantly covering the regions in front of and behind the shock. They start on DOY 333.2571 and DOY 333.5071, respectively (see Figure 7). The SWICS VDFs are shown in this figure with blue rectangles connected by green lines. The upper limits of integration are evident in both panels. The lower limits required additional attention. To determine the lower limits, we use the

procedure described in Section 3.2, i.e., fitting the core distributions with the kappa function (see Equation (3)). The fitting parameters are the following:  $g=5\times 10^8$ ,  $\kappa=4.93$ , and  $w=29.2~{\rm km~s^{-1}}$  upstream and  $g=1.70\times 10^9$ ,  $\kappa=2.65$ , and  $w=31.9~{\rm km~s^{-1}}$  downstream. The difference between the SWICS VDF and the corresponding kappa distributions is shown with blue triangles. In front of the shock, the PUI plateau lies at  $v^2f(v)=6.22\times 10^7~{\rm s~km^{-4}}$  between 192 and 502 km s<sup>-1</sup>. Behind the shock, it lies at  $v^2f(v)=2\times 10^8~{\rm s~km^{-4}}$  between 316 and 651 km s<sup>-1</sup>. We find that the pickup proton

density is  $2.85\times10^{-4}$  and  $2.38\times10^{-3}$  cm<sup>-3</sup> upstream and downstream, respectively. The corresponding temperatures are  $5.2\times10^6$  and  $10^7$  K.

The moments of the VDFs for pickup  $\text{He}^+$  (Figure 8) give us the upstream and downstream densities equal to  $1.3 \times 10^{-4}$  and  $2.84 \times 10^{-4}$  cm<sup>-3</sup>. The corresponding temperatures are  $3.5 \times 10^7$  and  $3.7 \times 10^7$  K, respectively.

It is of interest to compare these results with the test-particle analysis of the thermal and nonthermal ions crossing the observed structure of this shock (the details can be found in Gedalin et al. 2020). The bulk plasma and magnetic field parameters upstream of the shock are taken from Table 1. In particular, the ratio of the downstream magnetic field to its upstream value is  $B_{\rm d}/B_{\rm u}=2.6$  and the ratio of the maximum magnetic field in the overshoot (see Figure 6) is  $B_{\rm max}/B_{\rm u}=3.1$ . The upstream distribution is chosen as a combination of the kappa distribution with  $\kappa=4.9$ , w=29 km s<sup>-1</sup>, and the PUI plateau from  $v_1=192$  to  $v_2=502$  km s<sup>-1</sup>.

A detailed comparison of the distributions obtained in the test-particle analysis with the observed distributions is hardly possible. The test-particle distributions are just behind the shock front. They are strongly anisotropic because of the preferential heating in the direction perpendicular to the magnetic field. The secondary peak is due to the contribution of the reflected SW ions. The observed distributions are accumulated during 6 hr of further interaction of ions with the time-dependent fluctuations. The latter are expected to cause both smoothing out the peak and isotropization of the distribution. Nevertheless, there is a general agreement of the SW heating and PUI energization. Note, that the high-energy tail beyond the plateau was not included in the test-particle analysis.

Another way to look at the effects of shock is based on the diffusive shock acceleration theory (Drury 1983). Here we use the following formula to calculate the downstream particle VDF  $f_d$  using the upstream source particle distribution  $f_u$ :

$$f_d = \gamma v^{-\gamma} \int_{v_1}^{v} f_u(v') v'^{\gamma - 1} dv'. \tag{4}$$

Here the power slope of shock acceleration  $\gamma = 4.875$  is determined from the shock compression ratio. We assume that only particles above a certain threshold speed  $v_1$  are accelerated diffusively by the shock. The threshold speed is tuned until the downstream VDF reaches an appropriate intensity level, but its value does not affect the spectral shape. The result of the diffusive shock acceleration calculation using Equation (4) is shown in Figure 7 with the yellow line.

It can be seen that the prediction based on the diffusion shock acceleration theory does not match the observations. The slope of the high-speed tail above the cutoff speed is too flat. It could be because the shock compression ratio observed locally by Ulysses is too large and gives too much particle acceleration. The theoretical calculation produces a plateau in the spectrum; however, the intensity is too low compared to the observation, indicating too little acceleration in the plateau speed region. Adjusting the shock compression ratio cannot cure these two discrepancies together. While a decrease in shock compression will steepen the high-speed tail spectrum, it will also lower the plateau intensity. Additional physics must be involved to resolve this issue. We cannot exclude that the distribution of particles in the PUI velocity range is not nearly isotropic and causes the diffusive condition to fail.

#### 5. Discussion and Conclusions

Data from the Ulysses SWICS instrument provide us with a valuable information about the VDFs of ions, especially nonthermal (pickup) ions in the spacecraft frame. Equipped with the new methodology (Zhang et al. 2019) for converting these distributions to the SW frame, we were able to derive the properties of PUI protons and He<sup>+</sup> (density and temperature) over the period covering 2 months out of the long Ulysses lifetime of 18 yr. This time interval was chosen to include five CMEs, including a very famous Halloween event. It has been demonstrated that accurate approximation of the thermal ion distribution functions and their subtraction from the full distribution functions make it possible to identify the energy interval of PUIs, even if it is not clearly seen initially. Taking the moments of VDFs over velocity intervals containing PUIs allowed us to obtain the distributions of pickup protons and He<sup>+</sup> as functions of time along the Ulysses trajectory.

We showed that our new results are consistent, as far as the locations of major maxima and minima are concerned, with those obtained earlier in the narrow-beam approximation (Intriligator et al. 2012). However, our PUI density and temperature are noticeably higher. The reason is not only in the higher accuracy of the SWICS VDFs we used, but also in a more accurate determination of the PUI contribution to the full distribution functions. The latter improvement also allowed us to improve the integration limits for the PUI distributions. The agreement in the density values is better inside CME-related stream interaction regions.

Any observational data suitable for analyzing the behavior of nonthermal ions in the vicinity of collisionless shocks have additional value for space physics and plasma physics, in general. For this reason, we also used the measured VDFs for the analysis of pickup protons and He<sup>+</sup> at the shock that was crossed by Ulysses on DOY 333.5, 2003. This shock was chosen because it is located at the boundary between two 6 hr intervals of VDF accumulation. Observational data in front of and behind the shock provided by the MAG and SWOOPS instruments allowed us to determine the shock normal and speed. This gave us the full description of this shock from the MHD perspective. The properties of PUIs behind the shock are not described by the standard Rankine–Hugoniot conditions, so we obtained their properties from our analysis of SWICS data.

The SWICS electrostatic analyzer cycles through its voltage range approximately every 13 minutes. To decrease uncertainties related to instrumental effects, we accumulated VDFs within 6 hr intervals. This is better than the 12 hr windows used in Intriligator et al. (2012). However, the cadence of obtained VDFs did not allow us to investigate the modification of the PUI VDFs across the thin structure of this shock, which is determined by such kinetic processes as PUI reflection and acceleration. This is because the PUI VDF behind the shock contains information only on the resulting, averaged over 6 hr, properties of ions. Moreover, even the upstream VDF involves the averaged contribution of PUIs that were initially moving away from the shock but were forced to return by the motional electric field and ultimately cross the shock structure in the downstream directions. This can be seen from our test-particle simulations of ions crossing the shock structure shown in Figure 6. The distribution function behind the shock involves a peak related to reflected PUIs and cannot account for the isotropization that occurs within 6 hr. However, there is some general agreement with the SWICS distribution function except for the power-law tail, which cannot be described by testparticle simulations.

On the other hand, the effect of ion acceleration by this shock is very well seen in the result obtained with the diffusive shock acceleration theory, although the slope, being consistent with the theoretical expectation, is somewhat different from the one we see in data.

Our methodology was successfully tested and allowed us to eliminate the contamination of PUIs by the increased-speed thermal ions, especially in the vicinity of large gradients and shocks. This opens a path to the derivation of PUI properties for the entire Ulysses mission, which will further provide the heliospheric community with better understanding on the PUI behavior at heliocentric distances between 1 and 5 au. These results will also be of importance for validation of SW models involving PUIs. *IMAP* mission, scheduled for launch by NASA in 2025, will therefore benefit from such studies.

This work is a part of research supported by NSF-BSF grant 2010450. N.P., K.R., and T.K. were also supported by NASA grant 80NSSC18K1649. N.P. was additionally supported by the IBEX mission as a part of NASAs Explorer program. M.G. was partially supported by NSF-BSF grant 2019744 and by the European Union Horizon 2020 research and innovation program under grant agreement No. 101004131 (SHARP).

Ulysses SWICS data were obtained through https://nssdca.gsfc.nasa.gov. SWOOPS and MAG data were provided by CDAWeb at https://cdaweb.gsfc.nasa.gov. The authors are grateful to the instrument PIs George Gloeckler, David McComas, and Andre Balogh.

### **ORCID iDs**

Nikolai V. Pogorelov https://orcid.org/0000-0002-6409-2392

```
Ming Zhang  https://orcid.org/0000-0003-3529-8743
Michael Gedalin  https://orcid.org/0000-0003-1236-4787
Tae K. Kim  https://orcid.org/0000-0003-0764-9569
```

#### References

```
Burlaga, L. F., Ness, N. F., Belcher, J. W., et al. 1994, JGR, 99, 21511
Bzowski, M., Möbius, E., Tarnopolski, S., Izmodenov, V., & Gloeckler, G.
  2008, AA, 491, 7
Drury, L. O. 1983, RPPh, 46, 973
Gedalin, M., Pogorelov, N. V., & Roytershteyn, V. 2020, ApJ, 889, 116
Gedalin, M., Pogorelov, N. V., & Roytershteyn, V. 2021, ApJ, 910, 107
Gloeckler, G. 1990, RScI, 61, 3613
Gloeckler, G. 1996, SSRv, 78, 335
Gloeckler, G., Fisk, L. A., Geiss, J., et al. 2009, SSR, 143, 163
Gloeckler, G., Roelof, E. C., Ogilvie, K. W., & Berdichevsky, D. B. 1995,
   SSRv, 72, 321
Gruntman, M. A. 1982, SvAL, 8, 24
Intriligator, D. S., Detman, T., Gloecker, G., et al. 2012, JGR, 117, A06104
Kollmann, P., Hill, M. E., McNutt, R. L. J., et al. 2019, ApJ, 876, 46
McComas, D. J., Christian, E. R., Schwadron, N. A., et al. 2018, SSR, 214, 116
McComas, D. J., Swaczyna, P., Szalay, J. R., et al. 2021, ApJS, 254, 19
McComas, D. J., Zirnstein, E. J., Bzowski, M., et al. 2017, ApJS, 233, 8
Möbius, E., Hovestadt, D., Klecker, B., et al. 1985, Nat, 318, 426
Möbius, E., Lee, M. A., & Drews, C. 2015, APJ, 815, 20
Richardson, J. D., Kasper, J. C., Wang, C., Belcher, J. W., & Lazarus, A. J.
  2008, Nat, 454, 63
Richardson, J. D., Paularena, K. I., Lazarus, A. J., & Belcher, J. W. 1995, GRL,
   22, 1469
Richardson, J. D., & Smith, C. W. 2003, GRL, 30, 1206
Vasyliunas, V. M., & Siscoe, G. L. 1976, JGR, 81, 1247
von Steiger, R., Schwadron, N. A., Fisk, L. A., et al. 2000, JGR, 105, 27217
von Steiger, R., Zurbuchen, T. H., Geiss, J., et al. 2001, SSR, 97, 123
Wallis, M. 1971, NPhS, 233, 23
Wallis, M. K. 1975, Nat, 254, 202
Zank, G. P. 1999, SSR, 89, 413
Zank, G. P., Hunana, P., Mostafavi, P., & Goldstein, M. L. 2014, ApJ, 797, 87
Zhang, M., Zhao, L., von Steiger, R., et al. 2019, ApJ, 871, 60
```